# Strain and screening: Optical properties of a small-diameter carbon nanotube from first principles

Christian Wagner,[1,2,*] Jörg Schuster,[3,4] and André Schleife[2,5,6,†]

[1]*Technische Universität Chemnitz, Center for Microtechnologies, Reichenhainer Straße 70, 09126 Chemnitz, Germany*
[2]*Department of Materials Science and Engineering, University of Illinois at Urbana-Champaign, Urbana, Illinois 61801, USA*
[3]*Fraunhofer Institute for Electronic Nano Systems (ENAS), Technologiecampus 3, 09126 Chemnitz, Germany*
[4]*Dresden Center for Computational Materials Science (DCMS), Technische Universität Dresden, 01062 Dresden, Germany*
[5]*Frederick Seitz Materials Research Laboratory, University of Illinois at Urbana-Champaign, Urbana, Illinois 61801, USA*
[6]*National Center for Supercomputing Applications, University of Illinois at Urbana-Champaign, Urbana, Illinois 61801, USA*

Carbon nanotubes (CNTs) are a one-dimensional material system with intriguing physical properties that lead to emerging applications. While CNTs are unusually strain resistant compared to bulk materials, their optical-absorption spectrum is highly strain dependent. It is an open question, as to what extent this is attributed to strain-dependent (i) electronic single-particle transitions, (ii) dielectric screening, or (iii) atomic geometries including CNT radii. We use cutting-edge theoretical spectroscopy to explain strain-dependent electronic structure and optical properties of an (8,0) CNT. Quasiparticle effects are taken into account using Hedin's *GW* approximation and excitonic effects are described by solving a Bethe-Salpeter-equation for the optical polarization function. This accurate first-principles approach allows us to identify an influence of strain on screening of the Coulomb electron-electron interaction and to quantify the impact on electronic structure and optical absorption of one-dimensional systems. We interpret our thoroughly converged results using an existing scaling relation and extend the use of this relation to strained CNTs. We show that it captures optical absorption with satisfactory accuracy, as long as screening, quasiparticle gap, and effective electron and hole masses of the strained CNT are known.

## I. INTRODUCTION

Carbon nanotubes (CNTs) possess interesting material properties: their mechanical behavior is dominated by high stiffness and large rupture strain [1–5], they are chemically very stable [6,7], and show a sizable shift of electronic energy levels as a function of axial strain [8–12]. This shift renders *optical* transitions sensitive to strain, as has been observed experimentally [13–16] and explained theoretically [17]. For this reason, CNTs are excellent candidates for electronic and optical strain sensing and optical strain characterization, which is a promising technique due to the practical ease of optical readout and the higher precision compared to alternative approaches such as indirect electronic characterization. In particular, optical strain sensors with extremely high, mechanically tunable sensitivity can be built in combined CNT/micro-opto-electro-mechanical systems (MOEMS) [14,18–20].

Unfortunately, there is no simple, quantitative picture of the explicit strain behavior of optical transitions, since their dependence on the single-particle band gap of the CNT is not straightforward [17]. This can partly be attributed to strong many-body effects. In low-dimensional systems such as quasi-one-dimensional (1D) CNTs, there is less surrounding material than in bulk systems, leading to weak dielectric screening of the electron-electron and electron-hole interaction. As a consequence, quasiparticle (QP) shifts can be as large as 1.2 eV and excitonic effects can be equally strong [17,21–25]. However, in order to achieve precise strain sensing based on CNTs, a thorough understanding of electronic and optical properties, as well as their strain dependence, needs to be developed. Quantitative insight is essential for the development of MOEMS, such as strain-tunable emitters based on CNTs or tunable optical sensors.

On a more fundamental level, CNTs are a well-suited test bed for obtaining deeper insight into the physics of the strain dependence of screening and, hence, the screened Coulomb electron-electron interaction $W$. Understanding this is important for modern many-body perturbation theory, since in *GW* approximation (*GW*) and Bethe-Salpeter equation (BSE) calculations, $W$ plays a crucial role for the renormalization of electronic QP energies and optical transition energies. Large deformations are possible in CNTs before rupture, which allows exploring a much larger strain range than in bulk materials.

This understanding is also needed since difficulties often arise during the interpretation of experiments, e.g., for exciton binding energies. While in (homogeneous) bulk material, a spatial average is a good approximation that describes dielectric screening using a dielectric constant $\epsilon$, this cannot *a priori* be assumed for CNTs. The spatially resolved dielectric function $\epsilon(\mathbf{r}, \mathbf{r}')$ is needed because the material response, i.e., screening, is restricted to the actual electron density of the CNT [24] and is, thus, strongly direction dependent. In reciprocal space, spatial resolution corresponds to a

---
*Now at Helmholtz-Zentrum Dresden-Rossendorf, Bautzner Land-strasse 400, 01328 Dresden, Germany; christian.wagner@zfm.tu-chemnitz.de

†schleife@illinois.edu

dependence on $\mathbf{q} = \mathbf{k} - \mathbf{k}'$, which means that $\epsilon(\mathbf{q} = \mathbf{k} - \mathbf{k}')$ must be considered instead of a constant $\epsilon$. Dynamical screening is captured by the frequency-dependent dielectric function $\epsilon(\mathbf{q}, \omega)$, which is required when energy-dependent integrals occur.

Furthermore, as 1D materials, CNTs show negligible optical response perpendicular to the CNT axis, i.e., along the $z$ direction. Hence, screening $\epsilon(q_z = k - k')$ with $\mathbf{q} = q_z \mathbf{e}_z$ and Brillouin zone (BZ) sampling are effectively 1D. This needs to be taken into account when using analytical model functions to describe dielectric screening, since usually their $\mathbf{q}$ dependence is fitted to three dimensional (3D) semiconductors with a dielectric constant as low-$q$ limit [26]. However, in CNTs the low-$q$ (large distance) limit is vacuum screening [24,27]. Therefore the $q$ dependence of $\epsilon$ and the emerging local-field effects must be calculated accordingly. Nevertheless, in many studies only the dielectric constant $\epsilon$ is used as a screening model for the description of excitons in CNTs, since it is a much simpler quantity [22,28,29]. This neglect of local fields for the description of screening and the scaling of excitons in CNTs with respect to their radius, as proposed by Perebeinos *et al.*, [29], is an approximation that requires careful revision.

In this work, we use first-principles electronic-structure calculations to provide a deeper understanding of these questions. We use DFT [30,31] to compute ground-state geometries and total energies of a small-diameter (8,0)-CNT in equilibrium and under axial strain. Hedin's *GW* approximation [32] is used to account for QP effects on electronic energy levels. Using the $G_0W_0$ approximation, we derive strain-induced shifts of valence- and conduction-band energies and compare to results from a computationally cheaper hybrid exchange-correlation functional. Finally, by solving the BSE for the optical polarization function [33] we account for excitonic effects in optical-absorption spectra. We study the influence of Coulomb truncation, a scheme used to mitigate finite-size effects in supercell calculations for low-dimensional systems, on resulting optical spectra of the CNT under axial strain.

These detailed calculations of optical transitions allow us to disentangle the influence of strain on QP energies and on excitonic effects. Using our data, we explore whether the scaling relation by Perebeinos *et al.* [29], for the exciton binding energy in different CNTs, also holds for strain in a CNT. Finally, the relation between exciton binding energy, reduced effective mass, and dielectric constant is explored. The resulting strain dependencies of exciton binding energies and optical transitions are essential ingredients for design and layout of MOEMS.

The remainder of this work is structured as follows. Section II summarizes technical aspects of DFT, *GW*, and BSE calculations. In Sec. III, we use these techniques to discuss the strain-dependent electronic structure based on $G_0W_0$ and hybrid-functional calculations. The solution of the BSE is shown and exciton binding energies are analyzed. We then revisit the scaling relation of Ref. [29] and explore its applicability for the Coulomb-truncated case of a strained CNT. Finally, Sec. IV summarizes and concludes our work.

## II. THEORETICAL APPROACH AND COMPUTATIONAL DETAILS

### A. Ground-state properties

We use DFT [30,31] to compute total energies and, via minimization of Hellman-Feynman forces, optimized ground-state geometries of a (8,0)-CNT in equilibrium as well as under axial strain. For these calculations, the local-density approximation (LDA) is used to describe exchange and correlation [34] and the electron-ion interaction is described using norm-conserving pseudopotentials based on the parametrization by von Barth and Car [35]. Wave functions are expanded into a plane-wave basis up to a cutoff energy of 550 eV (40 Ry). To ensure accuracy, we also tested a plane-wave cutoff of 1100 eV (80 Ry), for which total energies are converged up to 9 meV/electron (36 meV/atom). In both cases, the resulting DFT as well as quasiparticle (QP) gaps agree within 20 meV, which we include in our error bars for QP energy calculations (see below). All DFT calculations are carried out using the QUANTUM ESPRESSO code [36].

We construct a simulation cell that contains the (8,0)-CNT, oriented along the $z$ axis and surrounded by vacuum in the other two directions. We choose a supercell size of $19.5 \times 19.5 \times 4.26$ Å$^3$, such that two periodic images of CNTs are separated by 13.2 Å. This is by far enough vacuum to obtain converged results and to suppress finite-size effects in DFT calculations for the neutral CNT. The geometry optimization is performed using a $1 \times 1 \times 20$ Monkhorst-Pack (MP) [37] $\mathbf{k}$-point grid and all atoms are relaxed until the remaining forces are smaller than 0.01 eV/Å. All our results for relaxed atomic geometries can be found in Ref. [38].

We then compare to calculations within the Vienna *ab initio* simulation package (VASP) [39,40]. For these we use the generalized-gradient approximation by Perdew, Burke, and Ernzerhof [41] and the projector-augmented wave method [42]. The calculations are carried out using a plane-wave cutoff energy of 400 eV and the same $\mathbf{k}$-point grid discussed above. Relaxed atomic geometries from both approaches differ only very slightly (GGA introduces about 0.2% strain, see Ref. [38]), which is reassuring for the comparison of excited-state properties below.

### B. *GW* calculations

In order to describe QP effects on electronic single-particle energies, we use Hedin's *GW* approximation for the electronic self energy [32]. We use the YAMBO package [43] to compute QP energies within one step of perturbation theory, i.e., without updating $G$ or $W$, which is known as $G_0W_0$ approach. The fully frequency-dependent dielectric response function $\epsilon(\mathbf{q}, \omega)$, that enters $W$, is computed within random phase approximation (RPA) using real-axis integration. Local-field effects play an important role and are converged for a $\mathbf{G}$-vector cutoff of 35 eV ($\approx$2.4 Ry), which results in less than 0.5% change of the dielectric function at several $\mathbf{q}$ points with respect to the extrapolated value or less than 20 meV change in the $G_0W_0$ gap (see Fig. 2 in Ref. [38]). Converged calculations require a $1 \times 1 \times 40$ MP $\mathbf{k}$-point grid ($1 \times 1 \times 60$ MP $\mathbf{k}$ points in case of Coulomb truncation, due

to the sharper profile of $\epsilon(q_z)$, see Ref. [21]) and at least 256 bands, which is four times the number of occupied states. Thus the default parameter set is 256 bands and 60 **k** points for *GW* calculations, unless other values are explicitly given. In addition, the singularity of the Coulomb integral in **k** space has to be circumvented, which is achieved using the random-integration method (RIM) described by Marini *et al.* [43], for *GW* calculations.

While the vacuum size in our supercell calculations is sufficiently large to achieve convergence in DFT, a thorough unit cell convergence is not feasible for the screened Coulomb interaction $W$, due to its long-range character. The slow decay of the Coulomb interaction with distance renders it impossible to eliminate artificial interactions between periodic images [44–47]. This can be compensated, e.g., when calculating defect-formation energies, by subtracting the electrostatic contribution of all repeating cells [45]. For converged calculations of $W$, Coulomb truncation schemes were developed [21,44], the YAMBO implementation of which is used in this work and described in Ref. [44]. Using this scheme renders a lateral unit cell size of 19.5 Å and a truncation cylinder for the Coulomb interaction (radius 9.75 Å) sufficient. All details on convergence tests for **k** points, number of bands, cell size, and Coulomb truncation, including the nontrivial convergence studies with YAMBO, are described in detail in Ref. [38].

### C. Bethe-Salpeter calculations

Excitonic effects are taken into account in the description of optical absorption by solving a BSE for the optical polarization function [33]. For BSE calculations, the screened electron-hole interaction $W$ is computed using the static limit of the response function and the same local-field effects as for *GW* calculations [43,48]. Ten valence and ten conduction bands are included for the solution of the BSE. Convergence with respect to **k** points is achieved using a $2 \times 2 \times 80$ MP grid and the same lateral unit cell size of 19.5 Å is found to be sufficient. These convergence tests are discussed in detail in Ref. [38]. The YAMBO package (version 3.4.2) is used for all *GW* and BSE calculations.

In order to better understand the influence of dielectric screening, we compare YAMBO results to BSE calculations from a recent VASP-based implementation [49,50]. These are carried out using the same parameters as for YAMBO: $2 \times 2 \times 80$ MP **k** points, ten valence and ten conduction bands, as well as the same simulation cell size. Local-field effects are included up to 35-eV **G**-vector cutoff, as discussed above for *GW* calculations. This allows calculating exciton binding energies that are converged to within about 1% with respect to the dielectric **G**-vector cutoff. This error estimate stems from the extrapolation of the estimated error of the dielectric function (see Fig. 2 in Ref. [38]). An accurate extrapolation scheme is used to circumvent the Coulomb singularity [50]. This BSE implementation currently does not support Coulomb truncation to remove the interaction between super cells, which is discussed in Sec. III E. In order to study the influence of the screened interaction $W$, we compare the results using a dielectric constant to an analytical model dielectric function [51] for screening. This comparison allows us to quantitatively discuss the
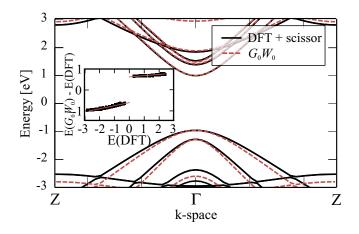


FIG. 1. $G_0W_0$ band structure (red dashed) is compared to scissor-shifted DFT results (black solid). Besides the scissor shift, the inset shows a linear dependence of quasiparticle (QP) shifts on KS eigenvalues. The fit shows that the *GW* valence band is stretched by about 1.15 and the *GW* conduction band by about 1.06 with respect to corresponding KS bands. The Fermi level of the *GW* band structure is chosen to be at zero energy.

interplay between Coulomb truncation, screening, and strain effects.

### III. RESULTS AND DISCUSSION

#### A. Electronic structure of the unstrained (8,0)-CNT

In Fig. 1, band structures computed using DFT (scissor-shifted to 1.84 eV) and $G_0W_0$ are compared. Our $G_0W_0$ gap of $1.84 \pm 0.02$ eV ($1.81 \pm 0.02$ eV when extrapolated to an infinite number of bands and **k** points, see Ref. [38]) agrees very well with early work by Spataru *et al.*, who reported 1.75 eV [21], and later work by Lanzillo *et al.*, who reported 1.81 eV [52]. The small difference to Spataru *et al.* [21] can be explained by slightly different computational parameters: they used the plasmon-pole approximation (PPA) to describe the $\omega$ dependence of the dielectric function and a slightly smaller 16-Å unit cell with Coulomb truncation beyond 7-Å cylinder radius.

The inset of Fig. 1 shows that $G_0W_0$ QP shifts depend approximately linearly on DFT Kohn-Sham (KS) eigenvalues. In addition to the scissor shift that opens up the gap, band stretching parameters $\beta$ describe the linear slope. We find that valence bands (VB) and conduction bands (CB) are stretched by $\beta_{vb} = 1.15$ and $\beta_{cb} = 1.06$. This implies a small correction of effective masses, $m^{GW} = \sqrt{\beta}\, m^{DFT}$, and needs to be taken into account when solving the BSE with much finer **k**-point sampling.

In order to calculate effective masses of the $\pi$ bands,[1] we use a hyperbolic fit that resembles the $G_0W_0$ bands as closely as possible [12]. The expression stems from the tight binding (TB) zone folding approach together with the Dirac cone

---

[1]Only the $\pi$ bands are optically active and their effective masses play an important role when comparing to results from BSE calculations.

approximation [53] for describing CNT band structures. The fit to DFT data yields effective masses of $m_{cb}^{DFT} = 0.422\,m_0$ for the conduction and $m_{vb}^{DFT} = 0.310\,m_0$ for the valence band. The effective masses of the respective $G_0W_0$ bands are $m_{cb} = 0.418\,m_0$ and $m_{vb} = 0.278\,m_0$, in quantitative agreement with band stretching.

## B. Hybrid functional for approximate QP energies

The QP correction of the DFT gap within the $G_0W_0$ approach is sizable: the extrapolated shift is $1.21 \pm 0.02$ eV, compared to a DFT gap of 0.60 eV. This large shift is attributed to weak dielectric screening in the 1D CNT, clearly indicating the need for using a QP correction scheme. Unfortunately, the $G_0W_0$ approach is computationally expensive and becomes unaffordable, e.g., when a large number of CNTs or many different strained configurations are studied. For these cases, an approximate description of QP corrections is beneficial and using a hybrid exchange-correlation functional, such as the one by Heyd, Scuseria, and Ernzerhof (HSE06) [54–56] has proven successful. It comes at much reduced computational cost, since no Coulomb truncation or expensive convergence with respect to empty states is needed. For the (8,0)-CNT, the reduction of cost is about a factor of 6.

The HSE06 functional contains 25% of Hartree-Fock (HF) exact exchange and leads to a band gap of 1.06 eV for the (8,0)-CNT. Increasing the fraction of HF exchange to 66% reproduces the $G_0W_0$ band gap (see details in Ref. [38]). Such a large fraction of HF exact exchange is not unusual for low-dimensional systems since screening is much weaker than in bulk materials, revealing almost bare electron-electron interaction. Clearly, using a hybrid exchange-correlation functional *without* adjusting the mixing parameter does not give correct band gaps for CNTs. As an example, the work of Matsuda *et al.* publishes a band gap of about 1.28 eV for the (8,0)-CNT, using the B3LYP functional without adapting the mixing parameter [57]. Next, we investigate whether the same fixed fraction of HF exchange results in sufficiently precise strain-dependent band gaps for the (8,0)-CNT, compared to $G_0W_0$ results.

## C. Electronic structure of the strained (8,0)-CNT

To investigate the strain dependence of the electronic structure, Fig. 2 shows fundamental gaps computed using DFT, modified HSE06, and $G_0W_0$, and band stretching parameters for several relative axial strains up to 6%. This illustrates the strong dependence of the fundamental gap on strain, which is significantly enhanced when QP effects are included, as seen from the different slopes of blue and green curves in the left panel of Fig. 2.

This effect can be understood by invoking strain-dependent dielectric screening, in addition to strain-dependent shifts of KS eigenvalues computed in DFT (blue curve in Fig. 2): The smaller the band gap of the strained CNT, the stronger the dielectric screening, and, thus, the weaker is the electron-electron repulsion. Since QP shifts are small in a material with strong dielectric screening, the $G_0W_0$ gap of the CNT with the largest axial strain (smallest gap) is closer to the DFT gap than for less strained CNTs.
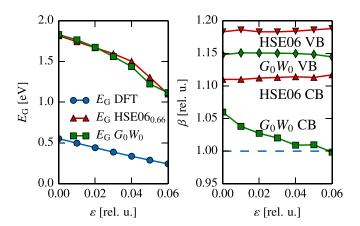


FIG. 2. (Left) Band gaps of DFT, $G_0W_0$, and modified HSE06 calculations (66% HF exact exchange) for the (8,0)-CNT under strain $\varepsilon$. (Right) Band stretching parameters $\beta_{CB,VB}$ of $G_0W_0$ and unmodified HSE06 calculations under strain (256 bands and $1 \times 1 \times 60$ **k** points). The blue dashed line indicates the DFT-LDA reference.

Figure 2 also illustrates that the band gap computed using the modified HSE06 functional with 66% exact exchange is very similar to the one computed using the $G_0W_0$ approach for all strains investigated here. The remaining difference is less than 0.1 eV, showing that axial strains up to $\approx 6\%$ have no influence on the required amount of HF exchange.

We also note that while band stretching $\beta$ differs between CB and VB, it only slightly changes with strain: $\beta_{cb}$ is reduced from 1.06 to 1.00 at 6% strain and $\beta_{cb}$ remains at a constant value of 1.15. The strain dependence of QP corrections modifies the strain-dependent effective mass of the CB by less than 3%. The VB is stretched by 15% (7% change of the effective mass), independent of the strain value. Overall, this means that the ratio of DFT and *GW* corrected effective mass is close to 1.0 and, thus, barely strain dependent. However, the absolute value of the effective mass [either from *GW* or from DFT] is strongly strain dependent as discussed in Sec. III F (see Fig. 6).

## D. Optical properties of the strained (8,0)-CNT

We now discuss the strain dependence of the optical spectrum via strain-induced shifts of the transitions $E_{11}$, $E_{22}$, $E_{33}$, and $E'_{11}$ as depicted in Fig. 3, where the index $nn$ indicates allowed transition from the $n$th $\pi$-VB to the $n$th $\pi$-CB [58]. The unprimed transitions denote first-order excitons, whereas the primed transition $E'_{11}$ is a second-order exciton ($n = 2$) that originates from the same electronic bands as $E_{11}$. This assignment relies on the numerical diagonalization of the exciton Hamiltonian, whose eigenstates are superpositions of noninteracting KS states. We analyzed these contributions for the different strained cases (see details in Ref. [38]) and our assignment agrees with Spataru *et al.* for the unstrained case [21]. In the following, results with and without Coulomb truncation are discussed and the origin of the exciton binding energy is investigated. The visualization of strain-dependent optical transitions in Fig. 4 shows that the first and second optical transition shift in opposite directions under strain. This is consistent with the most simple TB calculation of the
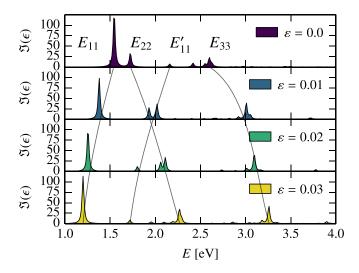
FIG. 3. Strain-dependent optical spectra of the (8,0)-CNT computed using the BSE approach with Coulomb truncation. The $E_{11}$ and $E'_{11}$ transitions shift to lower energies, whereas $E_{22}$ and $E_{33}$ shift to higher energies. $E'_{11}$ denotes a higher-order exciton ($n = 2$). Black lines are guides to the eye to highlight the shift of transitions.

CNT electronic bands with the zone-folding method applied to (strained) graphene [8], which predicts a downshift of CNT bands with strain for odd transitions ($n = 1, 3, \dots$) and upshifts of even CNT bands ($n = 2, 4, \dots$).

In contrast to this TB picture, we observe an upshift for the third optical transition that we attribute to $\sigma$-$\pi$ hybridization. Since the curvature of the (8,0)-CNT is large, $\sigma$ and $\pi$ bands hybridize and the respective band energies are lowered. This effect becomes stronger for higher bands and leads to reordering of the $n = 3$ and $n = 4$ states. As a consequence, the third optical transition shifts in the direction opposite to what is predicted by the zone-folding model, which does not include an effect of a curved CNT surface.

For the (8,0)-CNT, the first optical transition $E_{11}$, which is often observed in photo- or electroluminescence, appears in the infrared and shifts towards lower energies. For the unstrained CNT, we observe $E_{11}$ at $1.51 \pm 0.03$ eV, which is nearly identical to 1.55 eV reported by Spataru *et al.* [21]. We
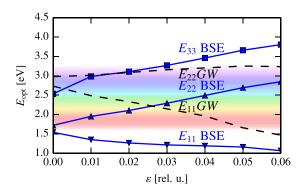


FIG. 4. Optical transition energies for the strained (8,0)-CNT with (BSE, blue solid) and without (GW, black dashed) excitonic effects, that shift strongly with applied axial strain, covering the visible spectral range.
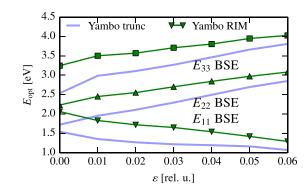


FIG. 5. The first three optical transitions computed with YAMBO using random-integration method (RIM) and homogeneous screening ("YAMBO RIM") for the 19.5-Å unit cell. For comparison, the result with Coulomb truncation is included ("YAMBO trunc").

explain the small difference with the slightly different gaps, the use of RPA instead of PPA, and the slightly smaller unit cell.

Under strain, the $GW$+BSE result for the $E_{11}$ transition shows a downshift to 1.02 eV at 6% tensile strain. Qualitatively, this trend follows the $GW$ results, but the exciton binding energy $E_{\mathrm{B}}$, defined as difference between $GW$ (dashed black line in Fig. 4) and $GW$+BSE transition (blue line with markers in Fig. 4), significantly reduces with strain. We explain this via the strain-induced increase of the dielectric constant, i.e., screening (see Fig. 6 and discussion in Sec. III F), that leads to a reduction of the exciton-binding energy.

The $E_{22}$ and higher transitions are observed in optical absorption, photoluminescence (PL) [15,58,59], Rayleigh scattering [60,61], and via photocurrents due to absorption [62–64]. Figure 3 illustrates that $E_{22}$ and $E_{33}$ each consist of a series of peaks. Their intensity-weighted average, depicted in Fig. 4, shows that $E_{22}$ and $E_{33}$ shift approximately linearly in energy with strain by a large value of about 200 meV/%. For larger strained armchair CNTs, such as (11,0) and (17,0), that show a reduced $\sigma$-$\pi$ hybridization, this value is only about 150 meV/% [17]. Since these CNTs should possess about the same strain dependence within the TB model with the zone folding scheme, it appears that the $\sigma$-$\pi$ hybridization itself is strain dependent. This leads to an enhanced strain sensitivity of electronic bands and corresponding optical transitions of the (8,0)-CNT.

### E. Exciton binding energies and long-range Coulomb interaction

In order to understand the physics of screening in strained CNTs, we compare BSE results with and without the Coulomb truncation scheme used for eliminating artificial Coulomb interactions of CNTs in adjacent super cells. We use YAMBO and the random-integration method (RIM) to solve the BSE for the untruncated case and compare to the truncated case in Fig. 5. We also compare to the VASP-BSE implementation, which uses a different solver [50] and find that both codes agree almost perfectly, as documented in Ref. [38].

Figure 5 shows that optical transitions appear at lower energies when the Coulomb interaction is truncated, which means that corresponding exciton binding energies are larger. While in the untruncated case the electron-hole interaction is (artificially) affected by periodic images over long distances, in the truncated case, no periodic images are present and only the much smaller vacuum screening contributes. Thus the truncation affects the low-$q_z$ behavior of $\epsilon(q_z)$, which determines the screening of the electron-hole interaction in the long-range limit. The reduction of screening for low $q_z$ due to Coulomb truncation explains the *enhancement* of exciton binding energies. Next, we establish detailed, quantitative insight into the scaling of exciton-binding energies with strain.

### F. Scaling of the exciton binding energy with strain

Figure 5 also illustrates that the energies of optical transitions for untruncated and truncated cases depend on strain and approach each other for large strain. The reason is that the band gap is reduced with increasing strain, leading to increased screening that even becomes metallic for about 9% strain. In the metallic case, the truncation has almost no effect on the, then very large, screening [21].

This effect of strain-dependent screening on exciton binding energy and *GW* gap does not just occur in 1D materials such as CNTs: The exciton binding energy in bulk ZnO decreases from approximately 70 to 55 meV between +2% and −2% strain due to different screening, see Ref. [65]. The effect is smaller in bulk, compared to low-dimensional systems, since screening is much stronger in 3D. For various 2D materials with band gaps less than about 2 eV, where screening effects are almost as strong as in CNTs, Zhang *et al.* showed that there is a simple, almost linear dependence of the exciton binding energy on the fundamental band gap [66]. They also showed that the absolute exciton binding energy is about 50% of the band gap and reported that it changes as the band gap changes, e.g., due to strain.

Next, we interpret the strain dependence of the exciton-binding energy via a scaling relation: Perebeinos *et al.* derived this for CNTs using a TB Hamiltonian together with an Ohno potential in order to solve the BSE [29]. By introducing a single parameter $\alpha$, they extended the well-known exciton scaling relation in homogeneous, isotropic materials [67], $E_B \sim \mu_{\text{eff}}\epsilon^{-2}$, to

$$E_B \approx A_B \mu^{\alpha-1} \epsilon^{-\alpha} r_{\text{CNT}}^{\alpha-2}, \tag{1}$$

where $A_B$ is the exciton-binding energy in a reference state, $r_{\text{CNT}}$ is the CNT radius, $\mu$ the reduced mass of electron and hole, and $\epsilon$ is the dielectric constant. Perebeinos *et al.* found a value of $\alpha = 1.40$ for $\epsilon > 4$ for CNTs. An independent confirmation of the parameter is given by Pedersen, who predicted a scaling of $E_B \sim r_{\text{CNT}}^{-0.6}$ using a variational approach for wave functions on a cylinder surface and homogeneous, background dielectric screening [22,28]. This result corresponds to the same value of $\alpha = 1.4$ and $\sim r_{\text{CNT}}^{\alpha-2}$. While the above relations were developed for a background dielectric screening, we now show that this screening (i.e., no Coulomb truncation) and local fields (i.e., with Coulomb truncation) are related.
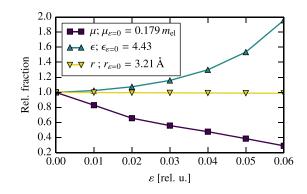


FIG. 6. Strain-dependent reduced effective mass, dielectric constant (for the 19.5-Å unit cell), and CNT radius. These parameters enter the scaling relation for the exciton binding energy, Eq. (1).

To analyze the validity of this scaling relation for CNTs under strain, we depict our first-principles results for the three materials parameters that enter Eq. (1) in Fig. 6. The dielectric constant is obtained from RPA calculations using YAMBO and the reduced effective mass results from our $G_0W_0$ data. This figure shows that the CNT radius depends only weakly on strain; the Poisson ratio of about 0.2 leads to a shift in the exciton binding energy of about 0.7% at 6% tensile strain. Conversely, the electronic structure is much more sensitive, leading to significant changes of effective masses and, via the fundamental gap, of the dielectric constant [8,9,11,12]. The two parameters $\mu$ and $\epsilon$, thus, determine the influence of strain on the exciton binding energy via Eq. (1).

In order to compare this to our BSE results, we depict the strain-dependent exciton-binding energy of the $E_{11}$ transition in Fig. 7. These data are computed using the strain-dependent dielectric function $\epsilon(q_z)$ for screening of the electron-hole interaction and we compare results based on Coulomb truncation (see Fig. 8) to those computed without the truncation scheme. As expected, the resulting exciton binding energies differ in magnitude, since the underlying screening models deviate between truncated and nontruncated case, especially for low $q_z$ (see Ref. [38]).
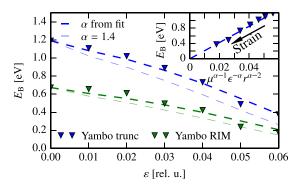


FIG. 7. Scaling of the strain-dependent exciton binding energy $E_B$ of the $E_{11}$ transition with ("YAMBO trunc") and without Coulomb truncation ("YAMBO RIM"). Symbols represent BSE results and dashed lines represent the scaling relation, Eq. (1), with different values of $\alpha$. The value of 1.40 given by Perebeinos *et al.* [29] is compared to a fit to BSE data. (Inset) Data for the Coulomb-truncated case as a function of the scaling parameter $\mu^{\alpha-1}\epsilon^{-\alpha}r^{\alpha-2}$.
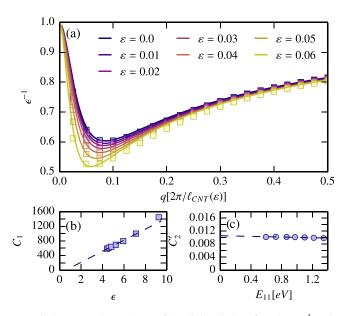
FIG. 8. In (a), the real part of the dielectric loss function $\epsilon^{-1}(q)$ is shown vs strain. Squares represent first-principles data with Coulomb truncation and lines represent the model fit using Eq. (2). (b) and (c) The fit coefficients $C_1$ and $C_2'$ as a function of $\epsilon$ and $E_{11}$, respectively.

More importantly, Fig. 7 illustrates that the scaling relation, Eq. (1), holds: fitting to results without Coulomb truncation yields a value of $\alpha \approx 1.29 \pm 0.03$ and shows almost perfect agreement with our data, despite the fact that BSE calculations take local-field effects into account, whereas Eq. (1) was derived under the assumption of a constant, homogeneous dielectric screening. Since there may be a significant influence from strong $\sigma$-$\pi$ hybridization due to CNT curvature, it is not surprising that the value of $\alpha$ slightly differs from 1.40 given by Perebeinos [29]. We note that the data in Fig. 7 were computed using YAMBO; VASP data are shown in Ref. [38].

Fitting to data with Coulomb truncation yields a slightly different value of $\alpha \approx 1.21 \pm 0.03$, since local-field effects with Coulomb truncation are not captured by the static, homogeneous screening entering the TB models used by Pedersen [22,28] or Perebeinos [29]. While this difference in $\alpha$ is, thus, not a surprise, it is remarkable that the scaling relation also holds in the Coulomb-truncated case, and we explore this in more detail in the next section. We point out that for this fit, we used the dielectric constant from the untruncated case (see Fig. 6) to mimic background screening, since Coulomb truncation would imply $\epsilon = 1.0$. This is also addressed in the next section, where we introduce a geometry-dependent parameter $C_1$ to substitute $\epsilon$ in the scaling relation. It characterizes the inhomogeneity and describes screening for confined carriers in the truncated geometry.

### G. Inhomogeneous dielectric screening and scaling relation

For a single CNT, as a localized, spatially inhomogeneous system, the wave-vector dependence of $\epsilon(q_z)$ is crucial when describing screening [21,24,46,68]. In order to incorporate this into the scaling relation, we use the analytic expression for the dielectric function of an infinite 1D cylinder, derived

by Deslippe *et al.* [24], using the Penn model [69]:

$$\epsilon_{1D}^{-1}(q_z) = 1 + \chi(q_z)\, v_{\text{trunc}}(q_z)$$

$$\approx 1 - C_2 \frac{R}{E_{11}} \frac{C_1 q_z^2}{1 + C_1 q_z^2} [2\, I_0(q_z R)\, K_0(q_z R)]$$

$$= 1 - C_2' R \frac{C_1 q_z^2}{1 + C_1 q_z^2} [2\, I_0(q R)\, K_0(q_z R)]. \tag{2}$$

Here, $C_1$, $C_2$, and $C_2' = C_2/E_{11}$ are constants and $R$ is the CNT radius. $I_0$ and $K_0$ are modified Bessel functions of the first and second kind, respectively. We fit this expression to our first-principles data for $\epsilon(q_z)$ in Fig. 8 and observe very good agreement. This means that the model of the 1D cylinder mimics screening in a CNT, once the influence of the supercell is removed via Coulomb truncation.

As shown in Fig. 8, the resulting fit parameter $C_1$ linearly depends on the strain-dependent dielectric constant $\epsilon$; $C_2'$ is strain independent. Therefore $C_1$ carries the strain dependence of the screening function that was described by $\epsilon$ before Coulomb truncation was applied. The relation between $C_1$ and $\epsilon$ is almost linear, which explains why the scaling relation, Eq. (1), also holds in the case of Coulomb truncation. We can, therefore, rewrite Eq. (1) using $C_1$ instead of $\epsilon$:

$$E_{\text{B}} = A_{\text{B}}\, r_{\text{CNT}}^{\alpha-2}\, \mu^{\alpha-1}\, C_1^{-\alpha}. \tag{3}$$

Hybrid DFT calculations can then yield effective masses and, after adjusting the fraction of exact exchange, strain-dependent corrected gaps. In combination with the RPA, these calculations also yield the inhomogeneous screening as a function of strain and, thus, the parameter $C_1$. This shows that for an isolated, strained CNT, the exciton-binding energy can be related to that of the unstrained state by means of a scaling relation, Eq. (3).

### IV. CONCLUSIONS

We use first-principles electronic-structure calculations, based on the $GW$+BSE approach, to compute strong, strain-related shifts of peaks $E_{\text{nn}}$ in the optical-absorption spectrum of an (8,0)-CNT, consistent with earlier literature. We find that the exciton binding energy in strained CNTs is a function of the band gap and our work leads to the important conclusion that this arises directly from strain-dependent inhomogeneous dielectric screening. This shows that deformation potentials of electronic eigenvalues *and* exciton binding energies need to be considered explicitly, in order to predict strain-dependent optical spectra of CNTs.

While this implies that the effect of many-body physics on optical spectra in strained CNTs is crucial, we then show that a more simple scaling relation for the exciton binding energy is applicable also to strained CNTs. This scaling relation allows us to extrapolate the shift of optical transitions from the unstrained state to the strained state, based on the strain-induced shift of electronic energy levels and the strain dependence of $\epsilon(q)$ and $\mu$. We then showed that the modified HSE06 hybrid functional, with a fraction of 66% exact exchange, mimics QP corrections for the unstrained CNT quite well, allowing us to avoid expensive $GW$ calculations of strained CNTs to determine these parameters.

Finally, we provide detailed understanding of why the scaling relation works for strained CNTs, even though it relies on the dielectric constant as a parameter and neglects the influence of local-field effects. To this end, we demonstrate that in low-dimensional materials, a wave-vector dependent screening function $\epsilon(q_z)$ must be used. In addition, in first-principles excited-state calculations, the Coulomb interaction must be truncated in order to obtain supercell convergence, which influences the long-range, low-$q_z$ part of the screening function. We show that a suitable screening function $\epsilon(q_z)$ for CNTs can be obtained from a 1D Penn model of a charge on an infinitely long, hollow cylinder and connect the parameters of this model to our first-principles data, leading to an excellent fit. We envision that this significantly advances the study of optical transitions in strained CNTs and enables broader applications of this interesting material system.

[1] Q. Lu and B. Bhattacharya, Nanotechnology **16**, 555 (2005).
[2] Y. Wu, M. Huang, F. Wang, X. M. H. Huang, S. Rosenblatt, L. Huang, H. Yan, S. P. O'Brien, J. Hone, and T. F. Heinz, Nano Lett. **8**, 4158 (2008).
[3] Z. Q. Zhang, B. Liu, Y. L. Chen, H. Jiang, K. C. Hwang, and Y. Huang, Nanotechnology **19**, 395702 (2008).
[4] J.-Y. Park, in *Carbon Nanotube Electronics* (*Integrated Circuits and Systems*), edited by J. Kong and A. Javey (Springer US, 2009), pp. 1–42.
[5] C. Pozrikidis, Arch. Appl. Mech. **79**, 113 (2009).
[6] A. Hirsch, Angew. Chem. Int. Ed. **41**, 1853 (2002).
[7] A. Förster, C. Wagner, S. Gemming, and J. Schuster, J. Vac. Sci. Technol. B **33**, 052203 (2015).
[8] L. Yang and J. Han, Phys. Rev. Lett. **85**, 154 (2000).
[9] A. Kleiner and S. Eggert, Phys. Rev. B **63**, 073408 (2001).
[10] E. D. Minot, Y. Yaish, V. Sazonova, J.-Y. Park, M. Brink, and P. L. McEuen, Phys. Rev. Lett. **90**, 156401 (2003).
[11] C. Wagner, S. Hartmann, B. Wunderle, J. Schuster, S. Schulz, and T. Gessner, in *2012 9th International Multi-Conference on Systems, Signals and Devices (SSD 2012), Chemnitz, Germany, 20–23 March 2012* (IEEE, Piscataway, NJ, 2012), p. 6198045.
[12] C. Wagner, J. Schuster, and T. Gessner, J. Comput. Electron. **15**, 881 (2016).
[13] P. Gopinath, A. Mohite, H. Shah, J.-T. Lin, and B. W. Alphenaar, Nano Lett. **7**, 3092 (2007).
[14] H. Maki, T. Sato, and K. Ishibashi, Nano Lett. **7**, 890 (2007).
[15] T. K. Leeuw, D. A. Tsyboulski, P. N. Nikolaev, S. M. Bachilo, S. Arepalli, and R. B. Weisman, Nano Lett. **8**, 826 (2008).
[16] M. Huang, Y. Wu, B. Chandra, H. Yan, Y. Shan, T. F. Heinz, and J. Hone, Phys. Rev. Lett. **100**, 136803 (2008).
[17] C. D. Spataru and F. Léonard, Phys. Rev. B **88**, 045404 (2013).
[18] C. Hierold, T. Helbling, C. Roman, L. Durrer, A. Jungen, and C. Stampfer, Adv. Sci. Technol. **54**, 343 (2008).
[19] B. R. Burg, T. Helbling, C. Hierold, and D. Poulikakos, J. Appl. Phys. **109**, 064310 (2011).
[20] T. Helbling, C. Roman, L. Durrer, C. Stampfer, and C. Hierold, IEEE Trans. Electron Devices **58**, 4053 (2011).
[21] C. D. Spataru, S. Ismail-Beigi, L. X. Benedict, and S. G. Louie, Phys. Rev. Lett. **92**, 077402 (2004).
[22] T. G. Pedersen, Carbon **42**, 1007 (2004).

[23] G. L. Zhao, D. Bagayoko, and L. Yang, Phys. Rev. B **69**, 245416 (2004).
[24] J. Deslippe, M. Dipoppa, D. Prendergast, M. V. O. Moutinho, R. B. Capaz, and S. G. Louie, Nano Lett. **9**, 1330 (2009).
[25] E. Malic, J. Maultzsch, S. Reich, and A. Knorr, Phys. Rev. B **82**, 035433 (2010).
[26] G. Cappellini, R. DelSole, L. Reining, and F. Bechstedt, Phys. Rev. B **47**, 9892 (1993).
[27] J. Jiang, R. Saito, G. G. Samsonidze, A. Jorio, S. G. Chou, G. Dresselhaus, and M. S. Dresselhaus, Phys. Rev. B **75**, 035407 (2007).
[28] T. G. Pedersen, Phys. Rev. B **67**, 073401 (2003).
[29] V. Perebeinos, J. Tersoff, and P. Avouris, Phys. Rev. Lett. **92**, 257402 (2004).
[30] P. Hohenberg and W. Kohn, Phys. Rev. **136**, B864 (1964).
[31] W. Kohn and L. J. Sham, Phys. Rev. **140**, A1133 (1965).
[32] L. Hedin, Phys. Rev. **139**, A796 (1965).
[33] G. Onida, L. Reining, and A. Rubio, Rev. Mod. Phys. **74**, 601 (2002).
[34] J. P. Perdew and A. Zunger, Phys. Rev. B **23**, 5048 (1981).
[35] A. Dal Corso, S. Baroni, R. Resta, and S. de Gironcoli, Phys. Rev. B **47**, 3588 (1993).
[36] P. Giannozzi, S. Baroni, N. Bonini, M. Calandra, R. Car, C. Cavazzoni, D. Ceresoli, G. L. Chiarotti, M. Cococcioni, I. Dabo, A. Dal Corso, S. de Gironcoli, S. Fabris, G. Fratesi, R. Gebauer, U. Gerstmann, C. Gougoussis, A. Kokalj, M. Lazzeri, L. Martin-Samos, N. Marzari, F. Mauri, R. Mazzarello, S. Paolini, A. Pasquarello, L. Paulatto, C. Sbraccia, S. Scandolo, G. Sclauzero, A. P. Seitsonen, A. Smogunov, P. Umari, and R. M. Wentzcovitch, J. Phys.: Condens. Matter **21**, 395502 (2009).
[37] H. J. Monkhorst and J. D. Pack, Phys. Rev. B **13**, 5188 (1976).
[38] See Supplemental Material at http://link.aps.org/supplemental/10.1103/PhysRevB.99.075140 for additional information, such as convergence studies and further details.
[39] G. Kresse and D. Joubert, Phys. Rev. B **59**, 1758 (1999).
[40] G. Kresse and J. Furthmüller, Phys. Rev. B **54**, 11169 (1996).
[41] J. P. Perdew, K. Burke, and M. Ernzerhof, Phys. Rev. Lett. **77**, 3865 (1996).
[42] P. E. Blöchl, Phys. Rev. B **50**, 17953 (1994).

[43] A. Marini, C. Hogan, M. Grüning, and D. Varsano, Comput. Phys. Commun. **180**, 1392 (2009).

[44] C. A. Rozzi, D. Varsano, A. Marini, E. K. U. Gross, and A. Rubio, Phys. Rev. B **73**, 205119 (2006).

[45] C. Freysoldt, P. Eggert, P. Rinke, A. Schindlmayr, and M. Scheffler, Phys. Rev. B **77**, 235428 (2008).

[46] F. Hüser, T. Olsen, and K. S. Thygesen, Phys. Rev. B **88**, 245309 (2013).

[47] D. Y. Qiu, F. H. da Jornada, and S. G. Louie, Phys. Rev. B **93**, 235435 (2016).

[48] M. Rohlfing and S. G. Louie, Phys. Rev. B **62**, 4927 (2000).

[49] C. Rödl, F. Fuchs, J. Furthmüller, and F. Bechstedt, Phys. Rev. B **77**, 184408 (2008).

[50] F. Fuchs, C. Rödl, A. Schleife, and F. Bechstedt, Phys. Rev. B **78**, 085103 (2008).

[51] F. Bechstedt, R. D. Sole, G. Cappellini, and L. Reining, Solid State Commun. **84**, 765 (1992).

[52] N. A. Lanzillo, N. Kharche, and S. K. Nayak, Sci. Rep. **4**, 3609 (2014).

[53] M. P. Anantram and F. Léonard, Rep. Prog. Phys. **69**, 507 (2006).

[54] J. Heyd, G. E. Scuseria, and M. Ernzerhof, J. Chem. Phys. **118**, 8207 (2003).

[55] J. Heyd, G. E. Scuseria, and M. Ernzerhof, J. Chem. Phys. **124**, 219906 (2006).

[56] A. V. Krukau, O. A. Vydrov, A. F. Izmaylov, and G. E. Scuseria, J. Chem. Phys. **125**, 224106 (2006).

[57] Y. Matsuda, J. Tahir-Kheli, and W. A. Goddard, J. Phys. Chem. Lett. **1**, 2946 (2010).

[58] S. M. Bachilo, M. S. Strano, C. Kittrell, R. H. Hauge, R. E. Smalley, and R. B. Weisman, Science **298**, 2361 (2002).

[59] Y. Ohno, S. Iwasaki, Y. Murakami, S. Kishimoto, S. Maruyama, and T. Mizutani, Phys. Rev. B **73**, 235427 (2006).

[60] M. Wang, L.-M. Peng, J. Y. Wang, and Q. Chen, Adv. Funct. Mater. **16**, 1462 (2006).

[61] K. Liu, J. Deslippe, F. Xiao, R. B. Capaz, X. Hong, S. Aloni, A. Zettl, W. Wang, X. Bai, S. G. Louie, E. Wang, and F. Wang, Nat. Nanotech. **7**, 325 (2012).

[62] M. Freitag, Y. Martin, J. A. Misewich, R. Martel, and P. Avouris, Nano Lett. **3**, 1067 (2003).

[63] N. M. Gabor, Z. Zhong, K. Bosnick, and P. L. McEuen, Phys. Rev. Lett. **108**, 087404 (2012).

[64] N. Rauhut, M. Engel, M. Steiner, R. Krupke, P. Avouris, and A. Hartschuh, ACS Nano **6**, 6416 (2012).

[65] A. Schleife, C. Rödl, F. Fuchs, J. Furthmüller, and F. Bechstedt, Appl. Phys. Lett. **91**, 241915 (2007).

[66] M. Zhang, L.-Y. Huang, X. Zhang, and G. Lu, Phys. Rev. Lett. **118**, 209701 (2017).

[67] H. Haug and S. W. Koch, *Quantum Theory of the Optical and Electronic Properties of Semiconductors*, 5th ed. (World Scientific, Singapore, 2009).

[68] F. A. Rasmussen, P. S. Schmidt, K. T. Winther, and K. S. Thygesen, Phys. Rev. B **94**, 155406 (2016).

[69] D. R. Penn, Phys. Rev. **128**, 2093 (1962).